



Exploration of photo-catalytic activity of nano-hydroxyapatite based on the crystallographic parameters: Estimation of crystallite size using X-ray diffraction data

Md. Sahadat Hossain^a, Shifa Sarkar^a, Sakabe Tarannum^{a,b}, Supanna Malek Tuntun^{a,b},
Monika Mahmud^a, Mashrafi Bin Mobarak^a, Samina Ahmed^{a,c,*}

^a Institute of Glass and Ceramic Research and Testing, Bangladesh Council of Scientific and Industrial Research (BCSIR), Dhanmondi, Dhaka, Bangladesh

^b Department of Applied Chemistry and Chemical Engineering, Noakhali Science and Technology University, Noakhali, Bangladesh

^c BCSIR Laboratories Dhaka, Bangladesh Council of Scientific and Industrial Research (BCSIR), Dhanmondi, Dhaka, Bangladesh

ARTICLE INFO

Keywords:

X-ray diffraction
Crystallography
Scherrer equation
Photocatalyst
Hydroxyapatite
Congo Red dye
Williamson-Hall plot

ABSTRACT

Nano-hydroxyapatite was synthesized from CaCO₃ and waste eggshells reacting with *ortho*-phosphoric acid, and titanium was doped to enhance the photocatalytic activity. The sample was characterized by X-ray diffraction technique, and different crystallographic parameters were explored focusing on crystallite size, microstrain, crystallinity index, lattice parameter, degree of crystallinity, microstrain, volume fraction of β-TCP, percentage of HAp, percentage of β-TCP, dislocation density, volume of unit cell, etc. To justify nano-crystallite size different models and equations such as the Williamson-Hall plot, linear straight -line model, Monshi-Scherrer model, Sahadat-Scherrer model, etc were employed. The effects of photocatalytic activity of synthesized hydroxyapatites were evaluated by varying the dye concentration, pH, interaction time, catalyst dose, and light source (halogen and sunlight). The photocatalytic activity was evaluated by degrading Congo Red dye and a relation was built between crystallographic parameters and catalysis. An easy degradation mechanism was also proposed for the Congo red dye using hydroxyapatite.

1. Introduction

Photocatalysts are the components with the ability to breakdown a wide range of chemicals (organic [1], petrochemicals [2], pharmaceuticals [3], etc.) and disinfect a wide variety of pathogens [4] (bacteria, viruses, fungi, and protozoan cells). As photocatalysts, several materials are used, including titanium dioxide (TiO₂), zinc oxide (ZnO), tin oxide (SnO₂), tungsten oxide (WO₃), cadmium sulfide (CdS), zinc sulfide (ZnS), cadmium selenide (CdSe), tungsten disulfide (WS₂), molybdenum disulfide (MoS₂), etc. [5,6]. One of the most promising uses of photocatalysts for water purification is advanced oxidation processes (AOPs) [7]. The nature, morphology, and concentration of the catalyst play crucial roles in the photocatalytic reaction process [8].

Hydroxyapatite is a phosphate-based bioceramic with the chemical formula Ca₁₀(PO₄)₆(OH)₂, and it can have either a monoclinic or hexagonal structure [9]. Hydroxyapatites are widely used in the biomedical sectors in their pure form or doped with different types of metal for enhanced biomedical properties [10]. It is a heterogeneous catalyst in

the broadest sense. In addition to moderate and complete oxidation [11], it is also used in the deposition of metals, dehydrogenation [12], the elimination of gaseous pollutants [13], the isotopic exchange of ¹⁸O₂ for ¹⁶O₂ [14], the transfer of hydrogen [15], and the treatment of wastewater [16]. Several forms of hydroxyapatite, including unmodified hydroxyapatite, modified hydroxyapatite, doped hydroxyapatite, and multiphasic hydroxyapatite, can be used to make them efficient photocatalysts. To alter the morphology and improve photocatalytic effectiveness, numerous synthesis techniques have also been explored. Its photocatalytic efficiency has been greatly improved by using transition metal replacement, biphasic preparation with metal oxide semiconductors, and powder composites [17]. Across the world, the textile industry is a major contributor to pollution due to the large volumes of wastewater effluents it discharges into the environment. The textile industry's wastes are widely recognized as being particularly hazardous due to the wide variety of toxic compounds they contain and pollution from these pollutants is harmful to aquatic life and should be avoided at all costs.

* Corresponding author.

E-mail address: shanta_samina@yahoo.com (S. Ahmed).

<https://doi.org/10.1016/j.jscs.2023.101769>

Received 10 October 2023; Received in revised form 27 October 2023; Accepted 5 November 2023

Available online 7 November 2023

1319-6103/© 2023 The Author(s). Published by Elsevier B.V. on behalf of King Saud University. This is an open access article under the CC BY-NC-ND license (<http://creativecommons.org/licenses/by-nc-nd/4.0/>).

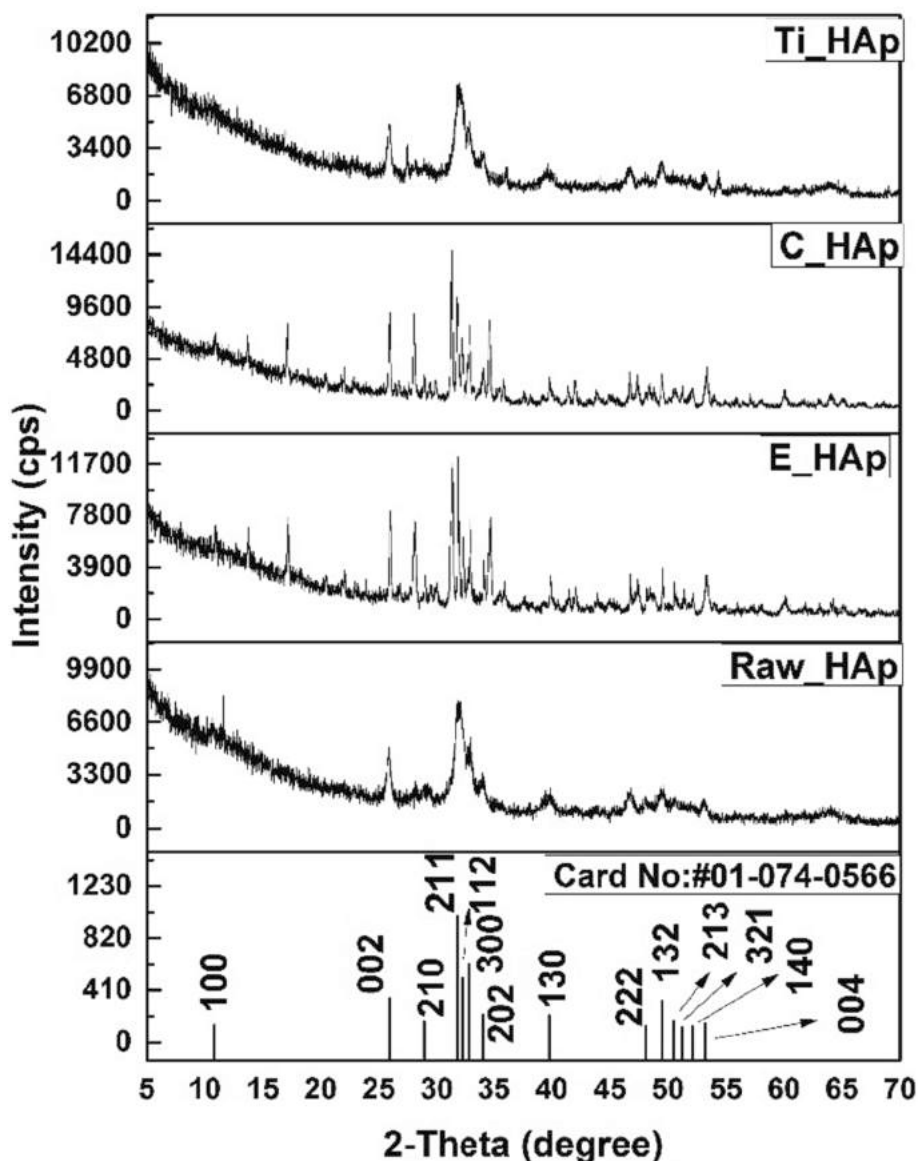


Fig. 1. XRD patterns of the Standard card (01–074-0566), and synthesized Raw_HAp, E_HAp, C_HAp, and Ti_HAp.

Table 1

Comparison of obtained and calculated data with standard JCPDS data (d in Å).

| Parameter | ICDD-HAp | Raw-HAp | C_HAp | E_HAp | Ti doped HAp |
|----------------------------------|--------------------------|--------------------------|--------------------------|--------------------------|--------------------------|
| hkl | d | d | d | d | d |
| 1 2 1 | 2.815 | 2.799 | 2.814 | 2.807 | 2.804 |
| 1 1 2 | 2.778 | 2.716 | 2.778 | 2.772 | 2.637 |
| 3 0 0 | 2.720 | 2.717 | 2.718 | 2.722 | 2.637 |
| Lattice parameter (Å) | a = b = 9.42 c = 6.88 | a = b = 9.41 c = 6.71 | a = b = 9.42 c = 6.88 | a = b = 9.40 c = 6.86 | a = b = 9.41 c = 6.85 |
| c/a | 0.7311 | 0.71 | 0.73 | 0.73 | 0.72 |
| Volume of cell (Å ³) | 529.09 | V = 514.62 | V = 528.67 | V = 524.74 | V = 525.88 |

Among them, dye pollution is easily observable since it is synthetic, has a complex structure, and is thus insoluble in water; it is also non-biodegradable and has a high biological oxygen need and chemical oxygen demand. There are about a hundred thousand different dyes available for purchase, and over 700,000 tons of dye are manufactured each year for application in textile industries [18]. This is due to the complex aromatic chemical structures of synthetic dyes, which have been linked to cancer and mutations. All over the world, nearly 1,000,000 tons of different types of dyes are used for various types of

industries such as food, tanneries, textile, medicinal sectors, and cosmetics [19].

fibers which causes severe pollution [20]. The textile dyeing sector is one of the worst offenders when it comes to excessive dye use [21]. Typically, 10–15 % of the dye remains unfixed during this procedure, and this percentage is subsequently discharged into the industrial effluent. As a result, 2–20 % of employed colors are released directly into aquatic bodies as aqueous effluents [22]. And, 80 % of the total environmental pollution caused by the textile industries is responsible for

Table 2
Different calculated crystallographic parameters of synthesized samples.

| Parameters | HAp | C_HAp | E_HAp | Ti doped HAp |
|---|--------|--------|--------|--------------|
| Crystallite size, nm | 9.28 | 56.96 | 16.56 | 5.58 |
| HAp percentage (%) | 100 | 100 | 100 | 100 |
| β -TCP percentage (%) | 0 | 0 | 0 | 0 |
| Volume fraction of β -TCP | 0 | 0 | 0 | 0 |
| Degree of crystallinity | 0.0196 | 4.5345 | 0.1106 | 0.0042 |
| Dislocation density, (10^{15} lines/ m^2) | 11.66 | 0.31 | 3.64 | 32.09 |
| Microstrain, ϵ | 0.78 | 0.13 | 0.42 | 1.29 |
| Crystallinity index, CI | 0.4352 | 0.1563 | 0.2937 | 0.2047 |
| Specific surface area, $S = (6 \times 1000) / (\text{density} \times \text{crystallite size}) \text{ m}^2/\text{g}$ | 205 | 33 | 115 | 324 |

untreated wastewater or weak effluent systems [23]. Nearly, 900 million tons of wastewater is discharged by the textile industries around the world [24]. Dyestuffs are the most difficult to remove from water among all organic molecules. Congo Red (CR) is an anionic dye with the chemical formula $C_{32}H_{22}N_6Na_2O_6S_2$ and the IUPAC designation benzidinediazo-bis-1-naphthylamine-4-sulfonic acid sodium salt [25]. CR isn't completely biodegradable and has been linked to health problems such as headedness, nausea, vomiting, and diarrhea [26]. Because of its great attractiveness for cellulose fibers, papermaking, cosmetics, pharmaceutical items, and plastic, this dye is also utilized in several other sectors, including the textile industry. These dyes, on the other hand, can't be removed from wastewater since they're water-soluble and resistant to chemicals and light. Colored wastewater discharge causes ecological toxicity and bioaccumulation of these dyes in marine species' bodies [27–29]. The presence of dyes in the effluent also limits the intensity of sunlight reaching the water's surface, which halts photosynthetic activity [30].

In this study, we synthesized a number of different types of hydroxyapatite, including both uncalcined (HAp) and calcined (C_HAp) varieties, as well as hydroxyapatite generated from eggshell (E_HAp) and hydroxyapatite doped with titanium (Ti-doped HAp). To get a comprehensive understanding of all the samples, a number of crystallographic characteristics and characterization procedures were

established. Congo red (CR) was used as a model dye, and we tested the photocatalytic activity of all of the synthesized samples by adjusting dye concentration, optimization of time, pH, and solar irradiation.

2. Materials and methods

2.1. Materials

Eggshells were purchased from a nearby local restaurant of BCSIR, Dhaka, Bangladesh. Calcium carbonate and titanium dioxide were bought from E-Merck Germany and no further purification process was engaged before using in the reaction. Ortho-phosphoric acid and nitric acid were purchased from Sigma-aldrich India.

2.2. Synthesis hydroxyapatites

For the synthesis of chemical hydroxyapatite (C_HAp), calcium carbonate and *ortho*-phosphoric acid were chosen as the raw sources of calcium and phosphate, respectively. The C_HAp was synthesized following the Ca/P ratio of 1.67 and the details procedure are reported elsewhere [31,32]. Hydroxyapatite was also synthesized from eggshells as the source of calcium and followed a similar method as C_HAp. Before calcination, the raw hydroxyapatite was mentioned as Raw-HAp, and after calcination at 900 °C for 30 min, the sample was marked as E_HAp. A prefixed amount of titanium dioxide was dissolved in nitric acid and the solution was added with the orthophosphoric acid for the preparation of 0.63 %Ti-doped hydroxyapatite (Ti-HAp). The reactions which are associated with the synthesis process are presented in equations 1–3.

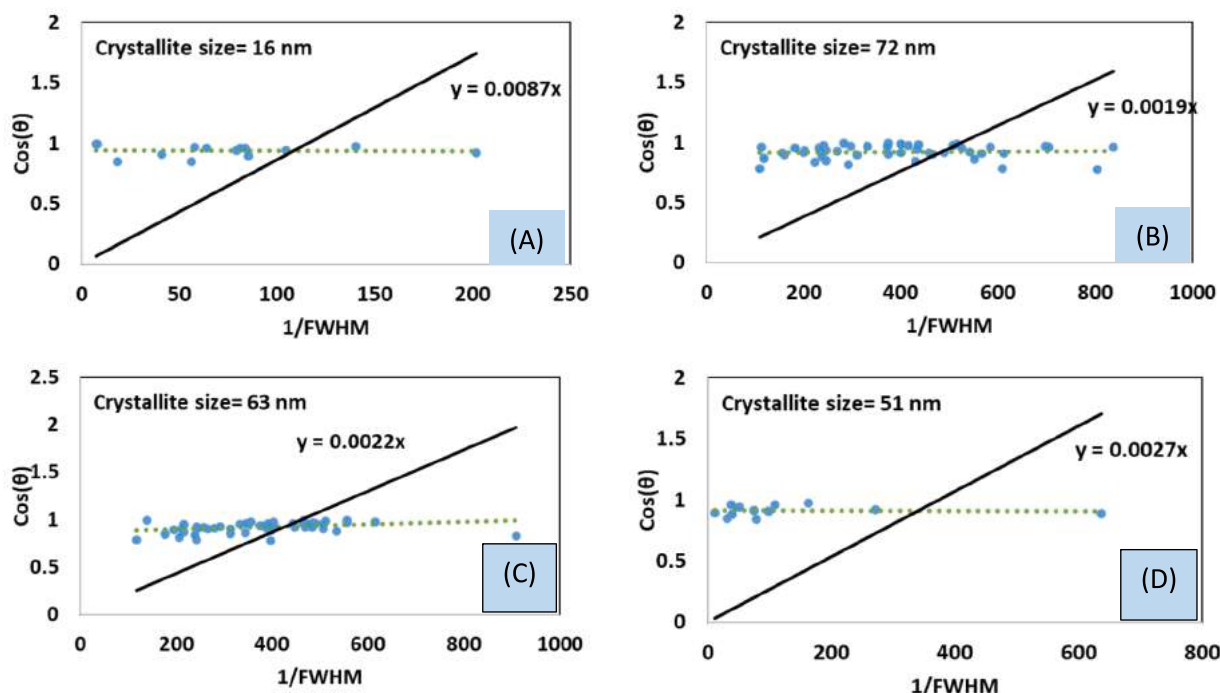


Fig. 2. Estimation of crystallite size using Sahadat-Scherrer model for (A) Raw HAp, (B) E_HAp, (C) C_HAp, and (D) Ti-doped HAp.

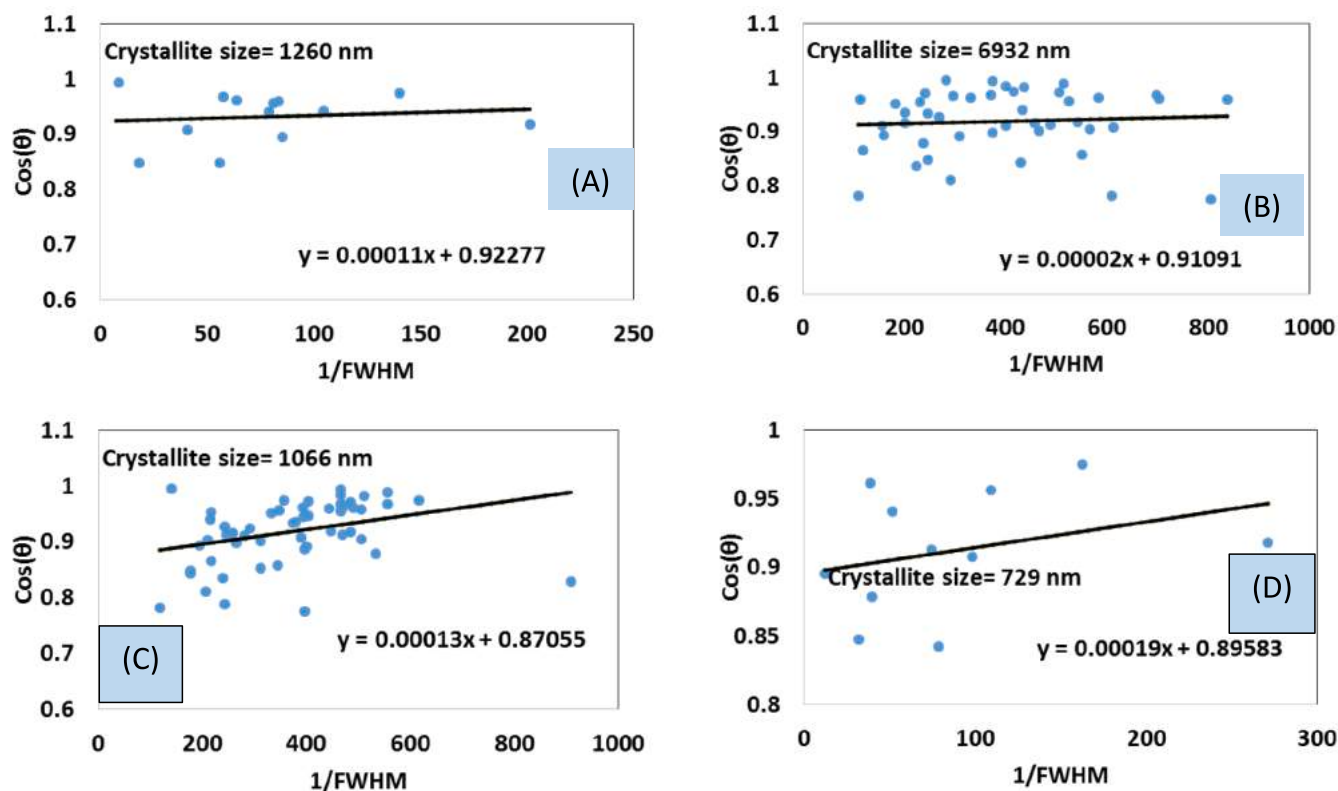


Fig. 3. Calculation of crystallite size from Linear Straight-line model for (A) Raw HAp, (B) E_HAp, (C) C_HAp, and (D) Ti-doped HAp.

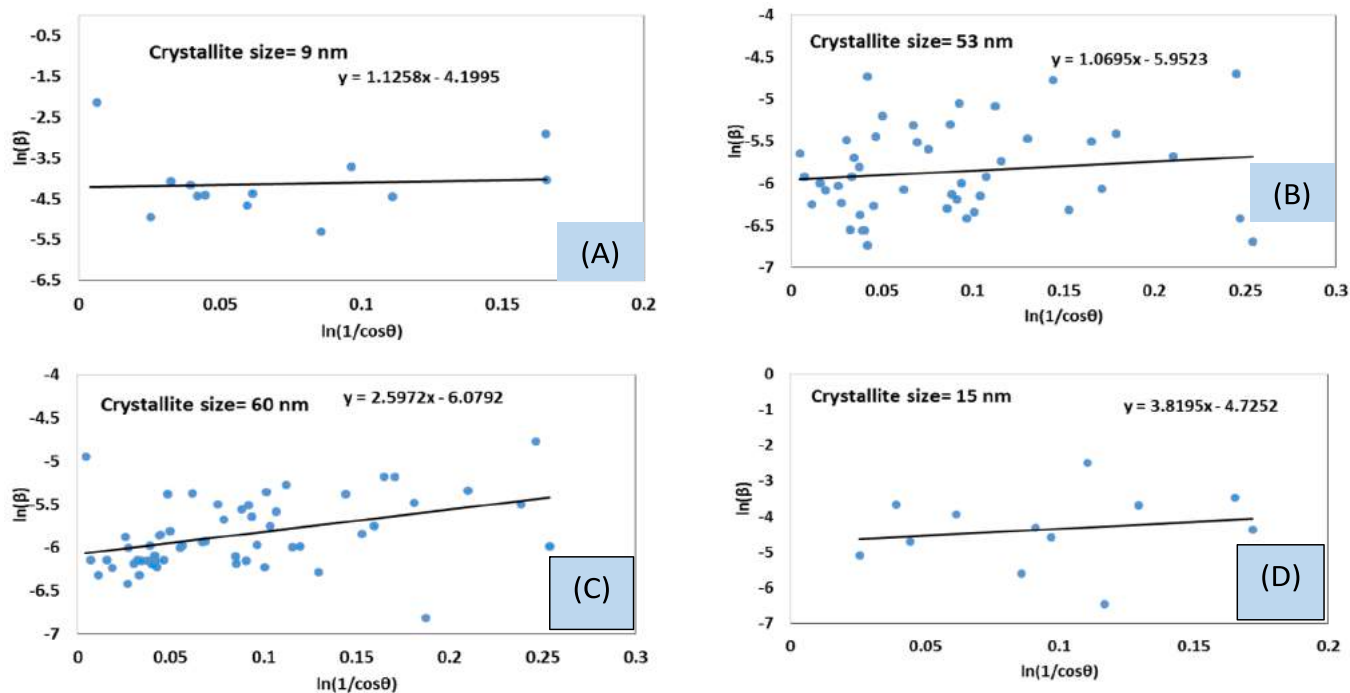


Fig. 4. Measurement of crystallite size using XRD data following Monshi-Scherrer method for (A) Raw HAp, and (B) E_HAp, (C) C_HAp, and (D) Ti-doped HAp.

2.3. X-ray diffraction (XRD)

The phase characterization of the produced powdered samples was carried out on a Rigaku SE XRD machine with a ceramic copper tube (Cu $K\alpha$, $\lambda = 1.54060 \text{ \AA}$) implanted as the radiation source. The data were

recorded from $2\theta = 5$ to 70° with steps of 0.01 and the temperature was kept between 19 – 20°C . The machine's voltage and current stayed at 40 kV and 30 mA, respectively. Before the sample was tested, the machine was set up with standard silicon. The gathered information was compared to the standard ICDD file (card no. 01-074-0566).

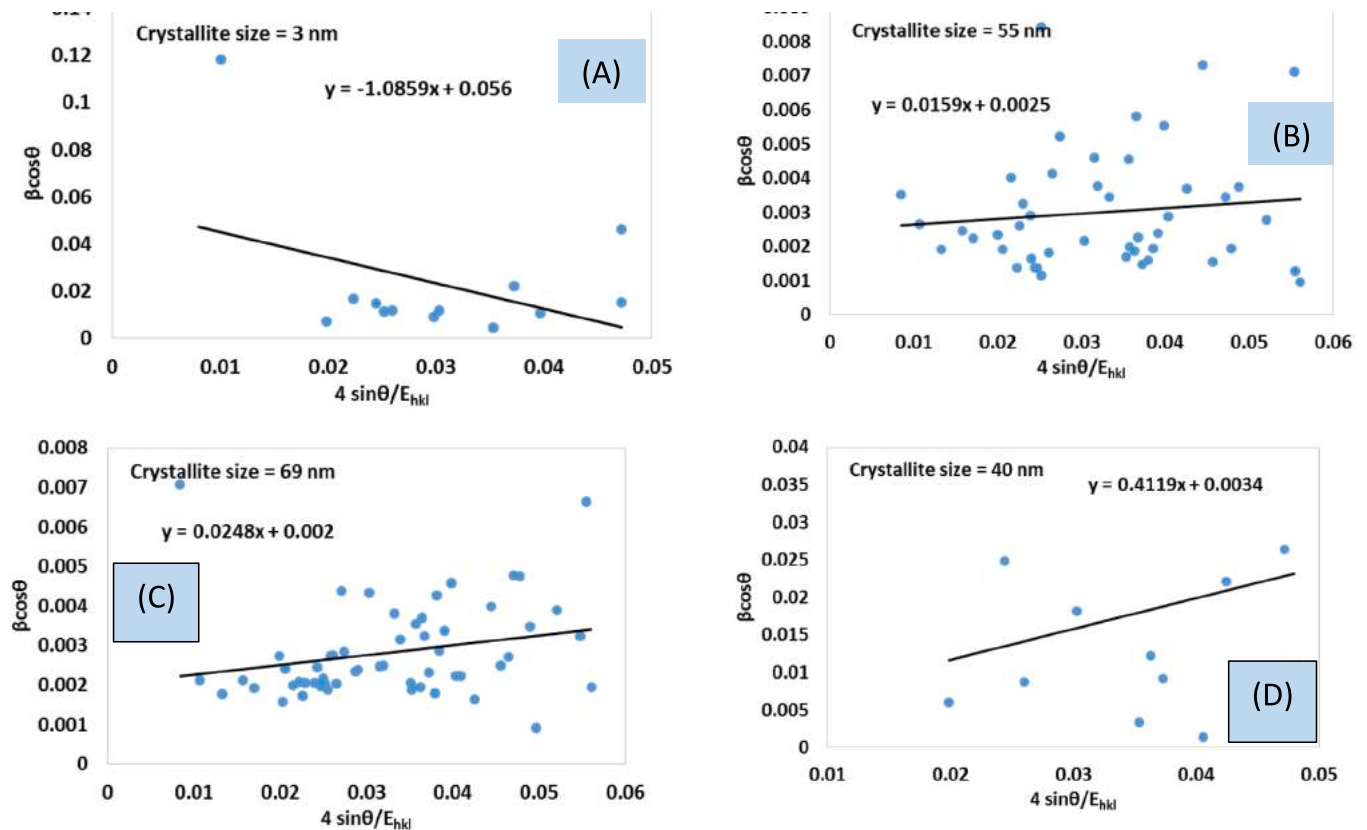


Fig. 5. Calculation of crystallite size using XRD data from Uniform Stress Deformation Model for (A) Raw HAp, (B) E_HAp, (C) C_HAp, and (D) Ti-doped HAp.

2.4. Catalytic activity

The catalytic activity of the synthesized samples was investigated using a halogen lamp (SEN TAI JM-500) of 500 W attached to a water bath. The experiment was performed maintaining a light-to-sample distance of 14 cm. The sample conditions were fixed at 20 ppm concentration, 50 mL volume, 25 °C temperature, neutral pH, 180 min light interaction time, and any change from these conditions were mentioned in the respective section. The photo-degradation percentage and photo-degradation capacity were computed by engaging equations 4, and 5. In equation 4, the D_p , C_o , and C_t represent the degradation percentage, initial dye concentration, and concentration at time t , respectively. Whereas, in equation 5, the degradation capacity, weight of the sample, and volume of the dye solution were indicated by q_e , w , and V , respectively.

$$\text{Degradation percentage, } D_p = \frac{C_o - C_t}{C_o} \times 100 \quad (4)$$

$$\text{Degradation capacity, } q_e = \frac{C_o - C_t}{W} \times V \quad (5)$$

3. Results and discussion

3.1. Crystallographic analysis

The X-ray diffraction patterns of synthesized samples are shown in Fig. 1, where cps is on the Y-axis and 2-theta (degree) is on the X-axis. The synthesized products were compared with the standard database (card no.: # 01-074-0566). In this case, the crystallographic investigation was performed by calculating the Crystallite size, Lattice parameter equation, Crystallinity index, Degree of Crystallinity, Microstrain, Volume fraction of β -TCP, Percentage of HAp, Percentage of β -TCP, Dislocation density, Volume of cell were calculated using eqn (6)-(15) and the

details of these equation are discussed elsewhere [33].

$$\text{Crystallite size, } D_c = \frac{K\lambda}{\beta \cos\theta} \quad (6)$$

$$\text{Lattice parameter equation, } \left(\frac{1}{d_{hkl}}\right)^2 = \frac{4}{3} \left(\frac{h^2 + hk + k^2}{a^2}\right) + \frac{l^2}{c^2} \quad (7)$$

$$\text{Crystallinity index, } CI_{\text{XRD}} = \frac{\sum H_{(202)} + H_{(300)} + H_{(112)}}{H_{(121)}} \quad (8)$$

$$\text{Degree of Crystallinity, } XC = \left(\frac{K_a}{\beta}\right)^3 = \left(\frac{0.24}{\beta}\right)^3 \quad (9)$$

$$\text{Microstrain, } \varepsilon = \frac{\beta}{4 \tan\theta} \quad (10)$$

$$\text{Volume fraction of } \beta\text{-TCP, } XB = \frac{PW_a}{1 + (P-1)W_a} \quad (11)$$

$$\text{Percentage of HAp} = \frac{I_{HA(121)}}{I_{HA(211)} + I_{\beta\text{-TCP}(0210)}} \quad (12)$$

$$\text{Percentage of } \beta\text{-TCP} = \frac{I_{\beta\text{-TCP}(0210)}}{I_{HA(211)} + I_{\beta\text{-TCP}(0210)}} \quad (13)$$

$$\text{Dislocation density, } \delta = \frac{1}{(D_c)^2} \quad (14)$$

$$\text{Volume of cell, } V = a^2 c \sin 60 \quad (15)$$

The definitions of the equations' symbols are as follows: The full width at half maximum (FWHM) in radians = β , the degree of diffraction angle = θ , the crystallite size = D_c , the shape factor is equal to Scherrer's constant, $K = 0.94$; Crystallographic lattice parameters are shown as a,

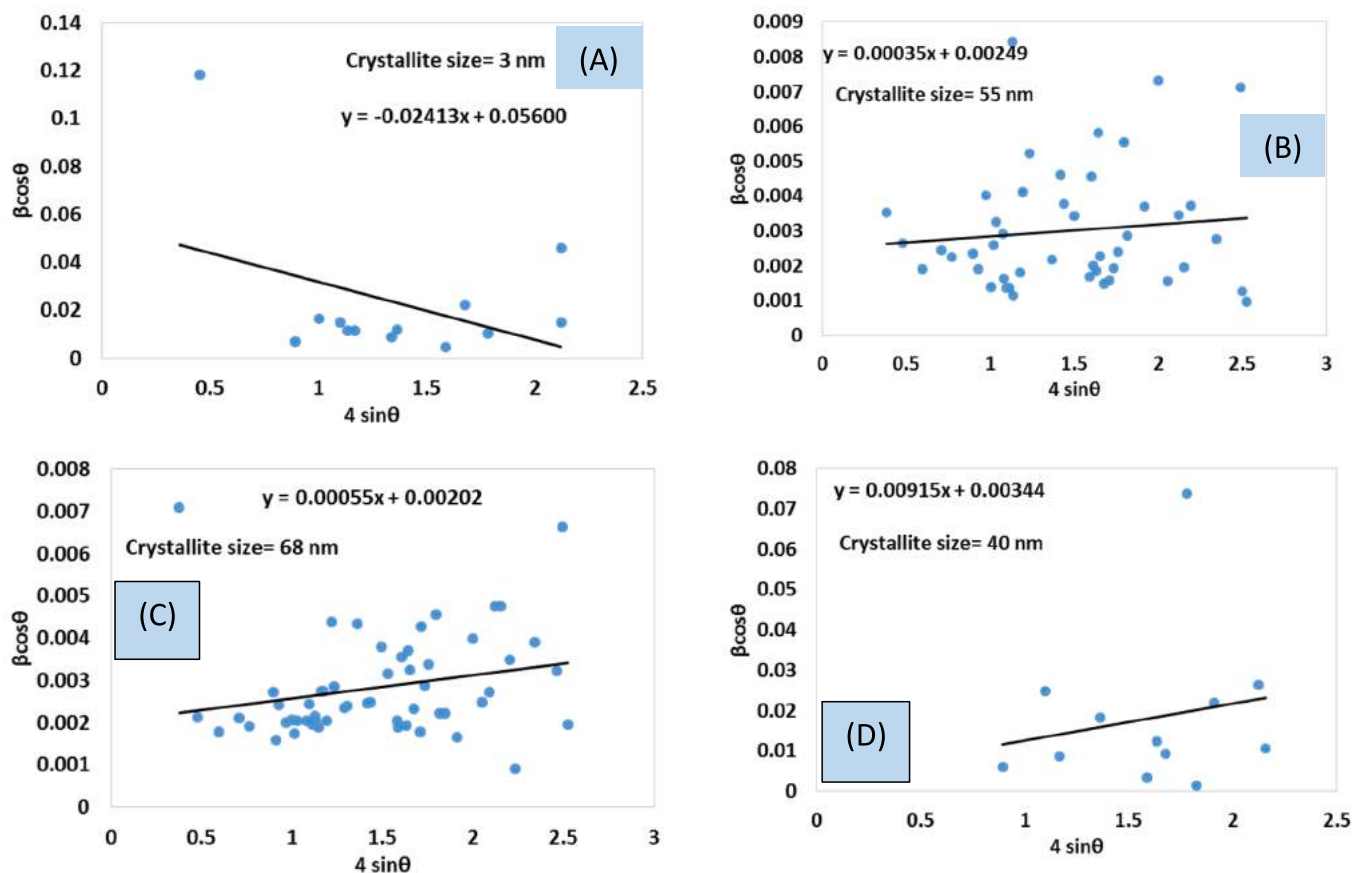


Fig. 6. Measurement of crystallite size using XRD data following Uniform Deformation Model for (A) Raw HAp, (B) E_HAp, (C) C_HAp, and (D) Ti-doped HAp.

b, and c; planes of the unit cell are shown as h, k, and l (in eqn (2)); peak height of the (hkl) plane = $H(hkl)$; K_a is a constant and the value for maximum HAp is 0.24; intensity of the β -TCP at (0210) plane = $I_{\beta\text{-TCP}(0210)}$ and for HAp = $I_{\text{HAp}(0210)}$; combined intensity of the HAp (121) reflection and the β -TCP (0210) reflection = $P = 2.275$; the percentage of β -TCP in eqn (7) = W_a and cell volume = V . Tables 1 and 2 contain a list of the calculated values.

3.2. Estimation of crystallite size

3.2.1. Sahadat-Scherrer model

The size of materials is widely considered for the application as a catalyst and also for other applications. The crystallite sizes of synthesized hydroxyapatites were evaluated by engaging Sahadat-Scherrer model as for this case the crystallographic planes were more than three. Equation 16 represents the mathematical expression of the Sahadat-Scherrer model and the details can be found elsewhere [34,35]. To build the graph from this model, $\cos\theta$ and $1/\text{FWHM}$ were plotted on the y-axis and x-axis respectively, and a straight line was built. Then, a second straight line was built by fixing the origin and a straight line was formed passing the origin. By comparing the formed equation with the standard formula of a straight line and equating slope of the equation 11 and the standard, the crystallite sizes were computed. Fig. 2 visualizes the Sahadat-Scherrer model for (A) Raw HAp, (B) E_HAp, (C) C_HAp, and (D) Ti-doped HAp. The crystallite size calculated from this model was inscribed inside the figure.

$$\text{Sahadat - Scherrer model, } \cos\theta = \frac{K\lambda}{D_{S-S}} \times \frac{1}{FWHM} \quad (16)$$

The crystallite size was lower in the case of uncalcined raw HAp, and increased due to the calcination.

3.2.2. Linear straight-line model

To evaluate the crystallite size the Linear straight-line model was also used which was built by reforming the Scherrer equation. Equation 14 represents the Linear straight-line model where the symbols carried the conventional significance, and the details of the equation were described elsewhere [33,36].

$$\text{Linear Straight - line model, } \cos\theta = \frac{K\lambda}{D_c} \times \frac{1}{\beta} = \frac{K\lambda}{D_L} \times \frac{1}{\beta} \quad (17)$$

To build the graph from this model, $\cos\theta$ and $1/\beta$ were plotted on the y-axis and x-axis respectively, and a straight line was built. By equating the built equation with the standard straight-line equation, the crystallite size was estimated and inscribed in the respective figure. Fig. 3 illustrates the Linear Straight-line model for (A) Raw HAp, (B) E_HAp, (C) C_HAp, and (D) Ti-doped HAp. The crystallite size computed from this model was too large to accept, thus this model was invalid for the investigating samples.

3.2.3. Monshi-Scherrer's method

Logarithm was taken on both side of the Scherrer equation and a new equation was formed which is widely familiar as the Monshi-Scherrer model. The mathematical expression of the Monshi-Scherrer model is shown in equation 16 and the details were published in a number of literatures [37,38].

$$\text{Monshi - Scherrer method, } \ln\beta = \ln \frac{1}{\cos\theta} + \ln \frac{K\lambda}{D_M} \quad (18)$$

Fig. 4 illustrates the Monshi-Scherrer method for (A) Raw HAp, and (B) E_HAp, (C) C_HAp, and (D) Ti-doped HAp. The inscribed crystallite size was within 100 nm and the crystallite sizes were higher when calcined at

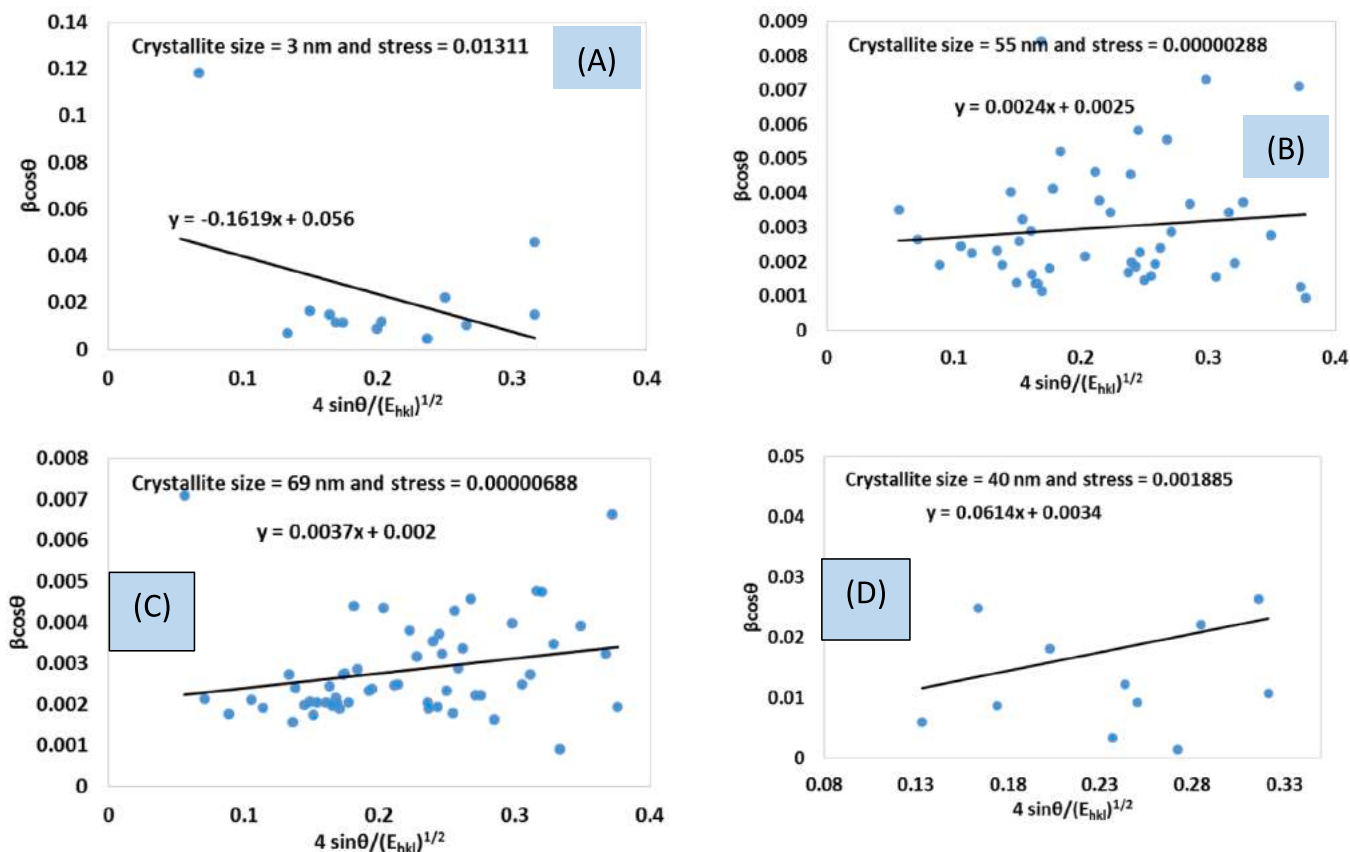


Fig. 7. Computation of crystallite size using XRD data using Uniform Deformation Energy Density Model for (A) Raw HAp, (B) E_HAp, (C) C_HAp, and (D) Ti-doped HAp.

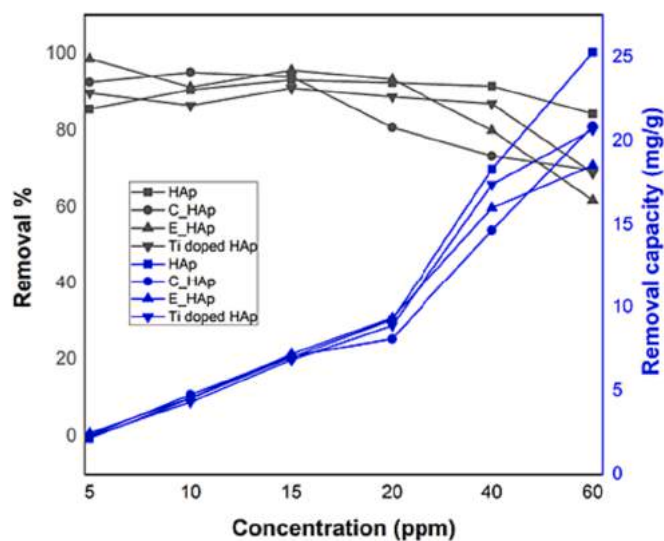


Fig. 8. Effect of initial concentrations of dye at a fixed time of 120 min and 0.1 g catalyst dose to estimate removal percentage and removal capacity for different types of synthesized hydroxyapatite.

high temperature.

3.2.4. Williamson–Hall plot

Considering the intrinsic strain in the crystals, the crystallite size was calculated from the Williamson–Hall plot using XRD data. The Stress deformation model, Uniform deformation model, and Energy

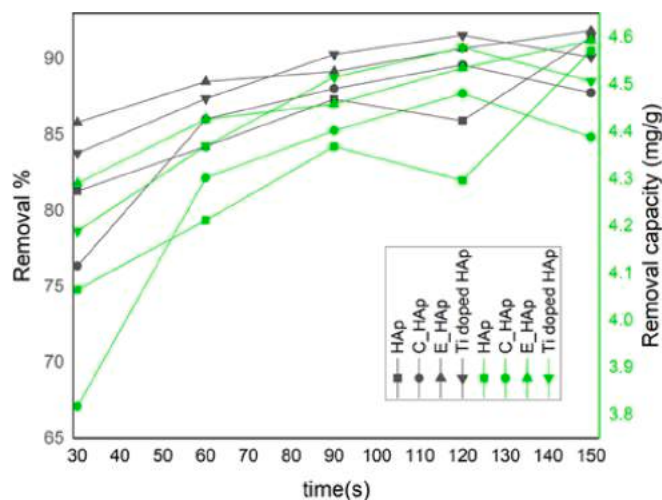


Fig. 9. Removal percentage and removal capacity of Congo Red at various exposure times for a fixed 0.1 g of catalyst dose, 10 ppm of dye concentration, and 120 min of time.

deformation model are mathematically expressed in equations 19, 20, and 21, respectively. The details of these models can be found elsewhere [39–41].

The mathematical expression of the Uniform Stress Deformation Model (USDM) is:

$$\beta_{\text{total}} \cos\theta = \frac{K_B \lambda}{D_{W-H}} + 4 \frac{\sigma}{E_{hkl}} \sin\theta \tag{19}$$

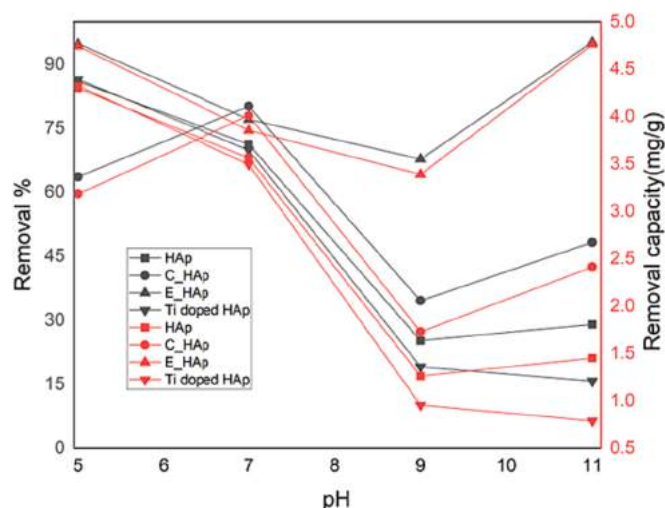


Fig. 10. Effect of pH variation on the removal percentage and removal capacity of Congo red dye for 0.1 g catalyst dose and an exposure time of 120 min.

The equation of Uniform Deformation Model (UDM) is:

$$\beta_{\text{total}} \cos \theta = \frac{K_B \lambda}{D_{W-H}} + 4 \epsilon \sin \theta \quad (20)$$

The Uniform Deformation Energy Density Model (UEDM) can be presented as:

$$\beta_{\text{total}} \cos \theta = \frac{K_B \lambda}{D_{W-H}} + 4 \left(\frac{2H}{E_{hkl}} \right)^{1/2} \quad (21)$$

Figs. 5–7 illustrated the Uniform Stress Deformation Model, Uniform Deformation Model, and Uniform Deformation Energy Density Model, tandemly for (A) Raw HAp, and (B) E_HAp, (C) C_HAp, and (D) Ti-doped HAp. In all the cases the crystallite sizes were within 100 nm and the size of crystals increased with the sintering temperature. The addition of titanium oxide also increased the crystallite size. The intrinsic strain was also calculated for the synthesized sample and inscribed along with the crystallite size in the respective figure.

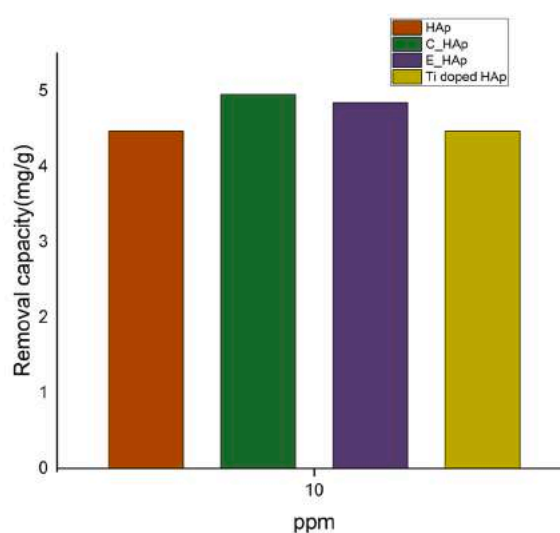
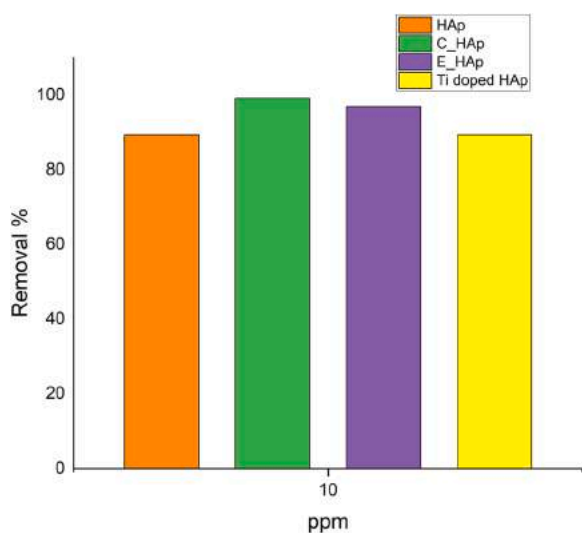


Fig. 11. Photodegradation of Congo red under the sunlight irradiation for a catalyst dose of 0.1 g at a dye concentration of 10 ppm, with a 120-minute exposure time.

3.3. Exploration of photocatalytic competency

3.3.1. Variation in dye concentration

The photocatalytic activity of the prepared samples was determined by using a range of dye concentrations (5–60 ppm) with a constant catalyst dose (0.1 g) and exposure time (120 min) (shown in Fig. 8). At low dye concentrations, such as 5, 10, 15, and 20 ppm, all of the samples performed admirably in terms of percentage and capacity for removing the dye. The eggshell-based adsorbent (E_HAp) proved particularly effective, removing 98 % of the dye at 5 ppm and 95 % at 15 ppm. A portion of the light may have been absorbed by the dye molecules when the reaction took place at a high concentration, which would have reduced the catalyst's photocatalytic activity. With the increased dye concentration, these samples had low dye removal efficiencies, except uncalcined HAp, which had the largest surface area compared to the calcined samples, resulting in the highest photocatalytic activity. At 40 and 60 ppm, uncalcined HAp had dye removal percentages of 91.4 %, and 84.3 %, and removal capacities of 18.3 mg/g, and 25.3 mg/g respectively.

3.3.2. Time optimization

In any degradation process, reaction time is an important factor. To optimize time, the amount of catalyst and concentration of dye used for degradation are crucial factors. It took less time to achieve efficient removal % and capacity values when a greater dose of catalyst was applied. However, as the catalyst concentration increases and the particles combine, the specific surface area is expected to decrease, resulting in decreased photocatalytic activity. An excess of suspended catalyst particles would obstruct the passage of UV light or sunlight, increasing light scattering and lowering photocatalytic efficacy [42]. However, at high dye concentrations, it takes longer to reveal the greater photodegradation rate, and this does not always occur because some light is absorbed by the dye molecules. According to Fig. 9, the rate of dye photodegradation rose considerably with increased exposure time. Yet, the photodegradation of the dye was almost identical at the longest times of 120 and 150 min. To take everything into account, 0.1 g of photocatalyst dose, 10 ppm of dye concentration, and 120 min were chosen for further experimental investigation.

3.3.3. pH variation

At a fixed catalyst dose of 0.1 g and an exposure time of 120 min, the pH, which ranges from 5 to 11, had a significant impact on all of the samples. It can be seen from Fig. 10 that all of the samples depicted outstanding degradation rates at low pH. This occurred due to the

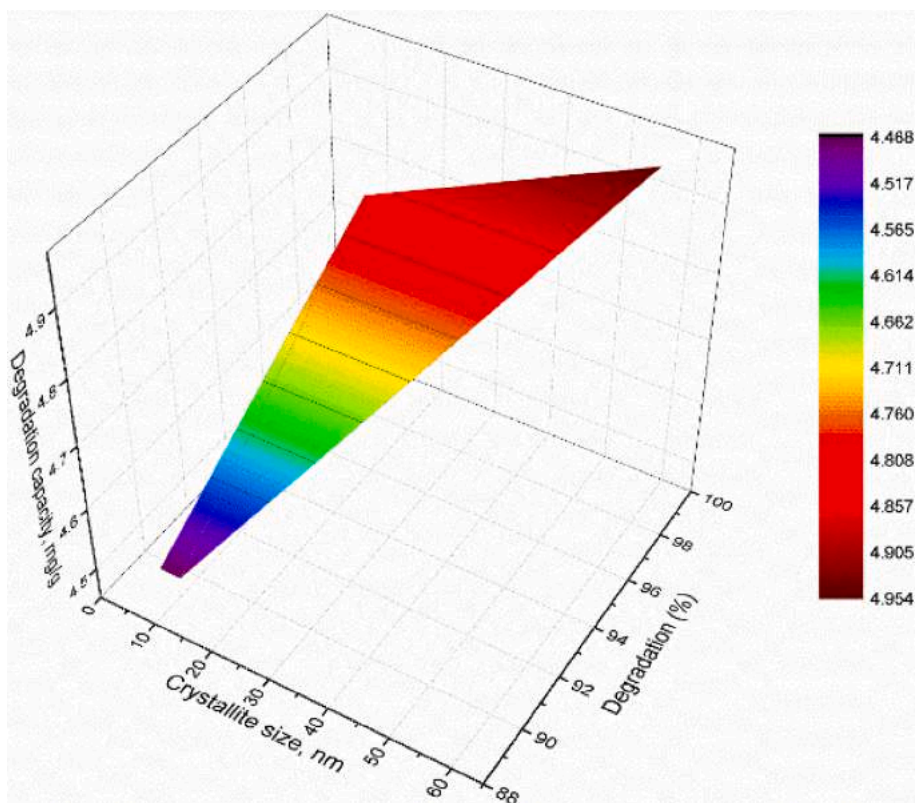


Fig. 12. Relation among crystallite size of synthesized hydroxyapatite, degradation percentage and degradation capacity for the degradation of Congo Red dye.

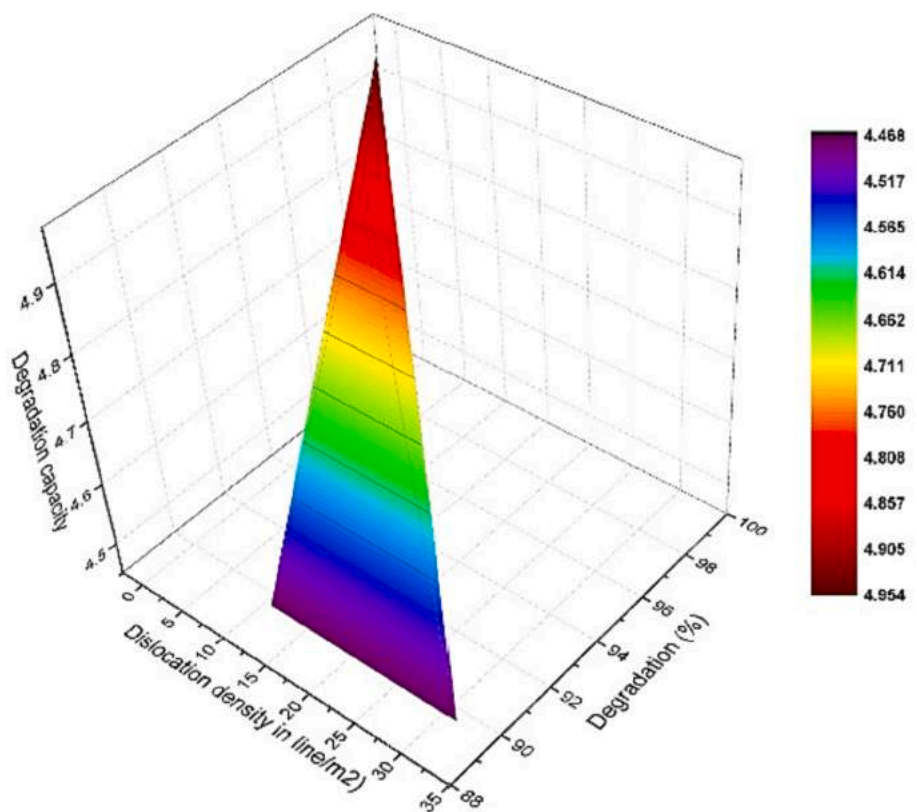


Fig. 13. Relation among dislocation density of synthesized hydroxyapatite, degradation percentage and degradation capacity for the degradation of Congo Red dye.

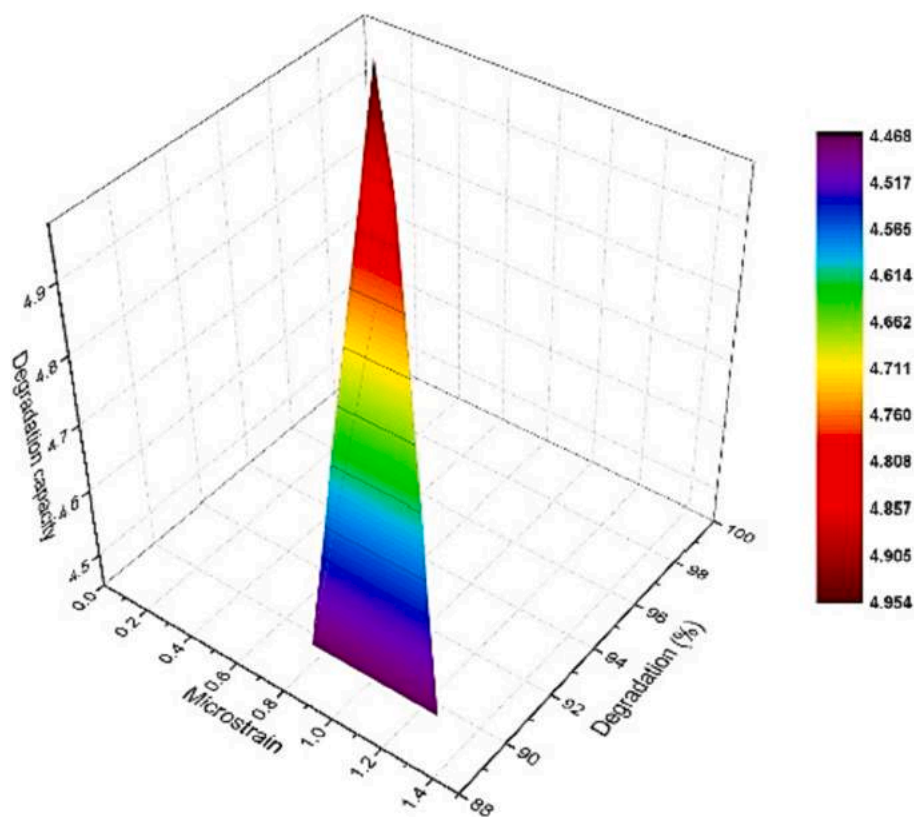


Fig. 14. Relation among microstrain of synthesized hydroxyapatite, degradation percentage and degradation capacity for the degradation of Congo Red dye.

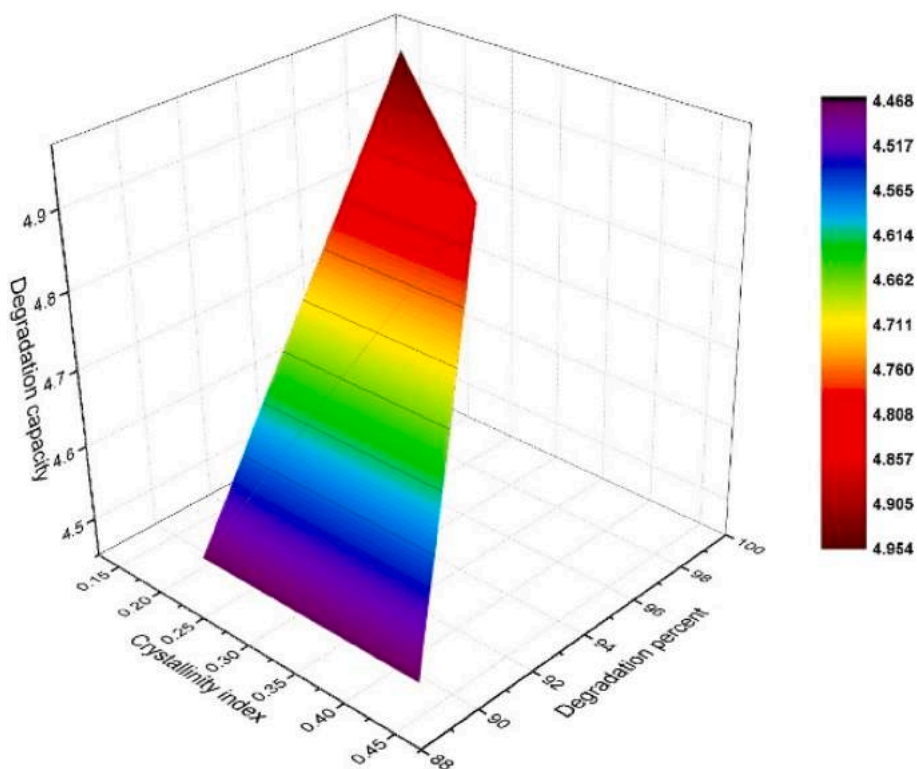


Fig. 15. Relation among crystallinity index of synthesized hydroxyapatite, degradation percentage and degradation capacity for the degradation of Congo Red dye.

anionic Congo red dye reacting with the amphoteric hydroxyapatite. Given that Congo red is an anionic dye with negatively charged sulfonic groups, it stands to reason that attractive forces would develop between

the dye substrate and the hydroxyapatite surface at low pH, where the greater number of H^+ ions on the hydroxyapatite surface would attract the negatively charged dye molecules, leading to high adsorption in an

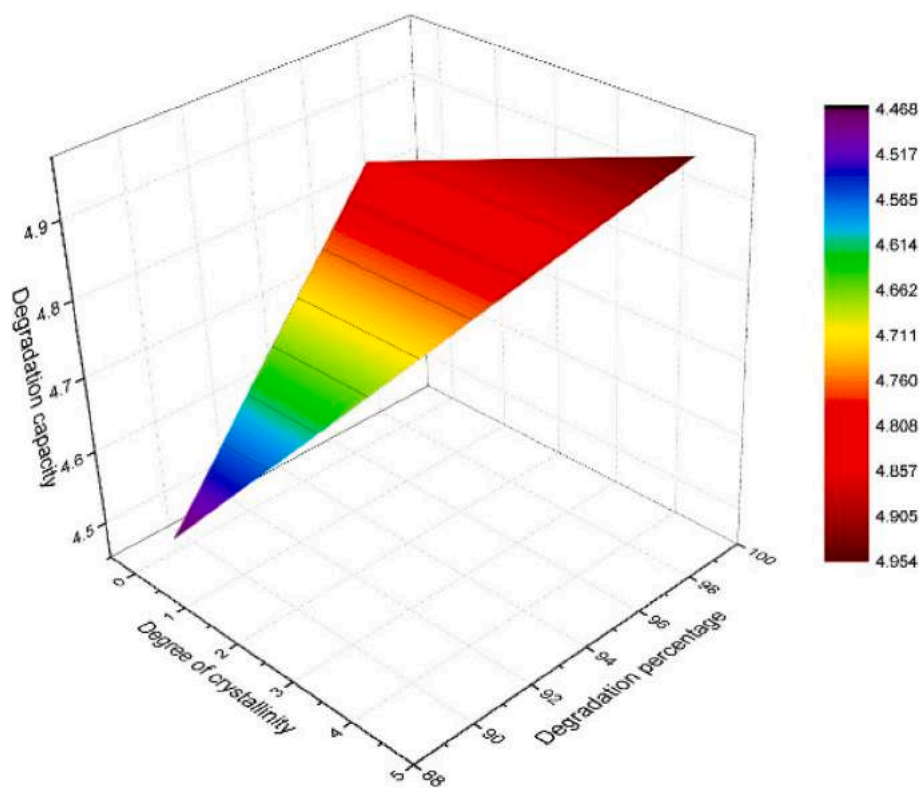


Fig. 16. Relation among degree of crystallinity of synthesized hydroxyapatite, degradation percentage and degradation capacity for the degradation of Congo Red dye.

acidic pH (5). The adsorption and degradation rates decrease as the pH rises because more and more OH ions are deposited on the hydroxyapatite surface, creating repulsive forces between the anionic Congo red and negatively charged hydroxyapatite surfaces because both surfaces have the same charge [43–45]. However, E_HAp demonstrated excellent results at pH 11, which is approximately 95 % removal percentage. This may have occurred as a result of its more rounded shape in a highly alkaline medium [46].

3.3.4. The response of photocatalyst under sunlight irradiation

Investigating how quickly the samples degraded in the presence of sunlight revealed unexpectedly outstanding results in comparison to those obtained using artificial visible light. The experiment was run based on the dye's removal percentage and removal capacity at a fixed catalyst dose of 0.1 g at a dye concentration of 10 ppm, with a 120-minute exposure time under sunlight (Fig. 11). C_HAp and E_HAp exceeded the other samples with removal percentages of 99 % and 96 %, as well as removal capacities of 4.95 mg/g and 4.85 mg/g, respectively. Even though solar radiation makes the degradation rate and capacity swing up, a 500-watt artificial light was used for the experiment because the intensity of sunlight changes depending on different factors. This makes it hard to estimate the photonic efficiency of products that have been synthesized. Furthermore, it is not practicable from an industrial aspect for industrial wastewater treatment without continuous light at all times of day and night.

3.3.5. Relation among the crystallographic parameters

Lower crystallite size was computed for the uncalcined HAp from the Scherrer equation as well as from all the model equations. However, the highest crystallite size was noticed for either C_HAp or E_HAp. The maximum degradation (~99 %) and capacity (4.95 mg/g) were computed for C_HAp but the crystallite size was not minimum. Fig. 12 represents the illustration of the crystallite size, degradation percentage, and degradation capacity of the synthesized samples. It can be predicted

from the relationship that the photocatalytic activity of the Congo Red dye was not governed by the crystallite size of the catalyst. And, the specific surface area was also minimum for the calcined HAp (shown in Table 1) thus the surface area was not also affecting the photocatalytic activity.

Dislocation is the imperfection in crystals and for crystalline material it is undesirable. The dislocation may be different types such as volume dislocation, area dislocation and line dislocation. In this case only line dislocation was computed from the equation and a relationship is visualized in Fig. 13. The minimum dislocation was noticed for C_HAp which was also responsible for the maximum percentage of Congo red dye degradation (and degradation capacity) by photocatalysis. On the other hand, maximum dislocation and minimum degradation percentage (and degradation capacity) were computed for Ti-HAp. Thus, imperfection in line with dislocation affected the photocatalytic activity of the synthesized sample.

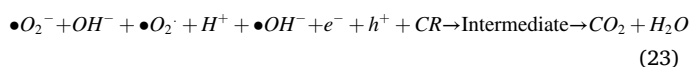
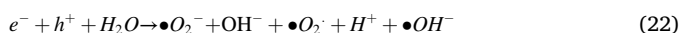
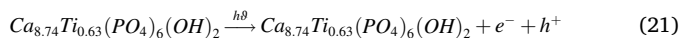
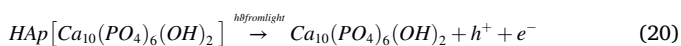
Microstrain also known as a local strain is normally generated by the distortion of lattice parameters and deviates from the standard crystals. The microstrain also influenced the photocatalytic activity of the synthesized products and the relationship among the microstrain, degradation percentage, and degradation capacity is pictured in Fig. 14. Minimum microstrain (0.13) was calculated for the C_HAp and the maximum photo-catalytic activity was also noticed for the same sample. The maximum microstrain lowered the degradation capacity for the Ti-HAp.

The dependency of degradation percentage, and degradation capacity on the crystallinity index is illustrated in Fig. 15. The crystallinity index was estimated from the three strong peaks which was mathematically presented in Equation 3. When the crystallinity index is minimum, the degradation percentage and degradation capacity were maximum which was obtained for the C_HAp. And, higher CI was responsible for the lower photo-catalytic activity.

The degree of crystallinity is another important crystallographic parameter that indicates the hardness, stiffness, and heat resistance of

any crystalline materials [32]. The effect of the degree of crystallinity on the degradation capacity and degradation percentage is shown in Fig. 16. It was noticed that the higher degree of crystallinity was responsible for the highest degradation percentage and degradation capacity. The C_HAP presented the highest degree of crystallinity (4.53) and the highest degradation percentage of Congo-red dye. The photocatalytic degradation of the Congo red dye depended on the degree of crystallinity instead of other conventionally reported parameters such as crystallite size and/or specific surface area and other parameters.

The reaction mechanism of Congo Red (CR) dye degradation can be represented as presented in equations 20–23, and a similar type of reaction mechanism has been reported elsewhere [31].



4. Conclusion

Four types of hydroxyapatites were synthesized successfully and their crystallographic characterization from XRD data was performed. Nano-crystallite size was justified using a number of model equations. Neither the crystallite size nor the specific surface area governed the photocatalytic activity of Congo Red dye for all the synthesized samples. Other crystallographic parameters such as microstrain, dislocation density, and crystallinity index could not influence the photocatalytic activity even certain percentage of Ti doping failed to enhance the activity. In this case, the degree of crystallinity governed the catalytic activity. From this research, it is suggested that in-depth crystallographic analysis should be performed for a better understanding of the governing parameter of the catalyst. The photo-catalytic activity of pure and doped hydroxyapatites showed variation due to the change in dye concentration, catalyst dose, pH, light source, time of interaction, etc. The chemically synthesized hydroxyapatite presented a higher degradation percentage and degradation capacity for the textile dye (Congo Red). Thus variation in crystallographic parameters can be a good tool for the degradation of different types of environmental pollutants.

Author contributions

Md. Sahadat Hossain conceived and designed the experiment, performed the characterization, analysed the data, wrote the original manuscript, and taken part in the experiment along with Shifa Sarkar. Shifa Sarkar synthesized samples, carried out the photocatalytic experiment. Sakabe Tarannum assisted in draft writing of the manuscript. Supanna Malek Tuntun assisted in Synthesizing Hydroxyapatite. Monika Mahmud assisted in sample synthesis. Mashrafi Bin Mobarak assisted in photocatalytic experiment. Samina Ahmed supervised the overall work and assisted writing the manuscript.

Declaration of competing interest

The authors declare that they have no known competing financial interests or personal relationships that could have appeared to influence the work reported in this paper.

Acknowledgements

The authors are grateful to Bangladesh Council of Scientific and Industrial Research (BCSIR), Dhaka-1205, Bangladesh authority for

financial support through R&D project (ref. no. 39.02.0000.011.14.134.2021/900; Date: 30.12.2021). Md. Sahadat Hossain acknowledge the financial support from the Ministry of Science and Technology, Bangladesh for approving R&D project (ref. no. 39.00.0000.012.20.011.22.56; date: 03.04.2023).

References

- [1] I.S. Hwang, et al., Hydrogen-treated TiO₂ nanorods decorated with bimetallic Pd-Co nanoparticles for photocatalytic degradation of organic pollutants and bacterial inactivation, *ACS Appl. Nano Mater.* 6 (3) (2023) 1562–1572, <https://doi.org/10.1021/acsnm.2c04160>.
- [2] X. Duan, et al., Photocatalytic degradation of VOC waste gas in petrochemical sewage fields, *Ind. Eng. Chem. Res.* 61 (51) (2022) 18676–18684, <https://doi.org/10.1021/acs.iecr.2c03272>.
- [3] F. Sharmin, M.A. Basith, Highly efficient photocatalytic degradation of hazardous industrial and pharmaceutical pollutants using gadolinium doped BiFeO₃ nanoparticles, *J. Alloy. Compd.* 901 (2022), 163604, <https://doi.org/10.1016/j.jallcom.2021.163604>.
- [4] L.V. Bora, Solar photocatalytic pathogenic disinfection: fundamentals to state-of-the-art, *Water Sci. Eng.* (2022), <https://doi.org/10.1016/j.wse.2022.12.005>.
- [5] H. Singh, A. Bokare, A. Kumar, R. Trehan, A. Sharma, D. Kumar, Chapter 6 - Formation of magnetite-based ceramic materials and their photocatalytic applications, *Elsevier Series on Advanced Ceramic Materials*, in: S. Singh, P. Kumar, D.P. Mondal (Eds.), *Advanced Ceramics for Versatile Interdisciplinary Applications*, Elsevier, 2022, pp. 115–146.
- [6] Y. Liu, et al., Metal or metal-containing nanoparticle@MOF nanocomposites as a promising type of photocatalyst, *Coord. Chem. Rev.* 388 (2019) 63–78, <https://doi.org/10.1016/j.ccr.2019.02.031>.
- [7] A.O. Oluwole, E.O. Omotola, O.S. Olatunji, Pharmaceuticals and personal care products in water and wastewater: a review of treatment processes and use of photocatalyst immobilized on functionalized carbon in AOP degradation, *BMC Chemistry* 14 (1) (2020) 62, <https://doi.org/10.1186/s13065-020-00714-1>.
- [8] A. Ojha, in: Chapter 19 - Nanomaterials for Removal of Waterborne Pathogens: Opportunities and Challenges, *Butterworth-Heinemann*, 2020, pp. 385–432, <https://doi.org/10.1016/B978-0-12-818783-8.00019-0>.
- [9] F. Chiatti, M. Corno, P. Ugliengo, Stability of the dipolar (001) surface of hydroxyapatite, *J. Phys. Chem. C* 116 (10) (2012) 6108–6114.
- [10] L. Omar Ahmed, et al., Exploring the electronic band structure, spectroscopic signatures, and structural properties of Er³⁺-based hydroxyapatites co-doped with Ce³⁺ ions, *Inorg. Chem. Commun.* 155 (2023), <https://doi.org/10.1016/j.inoche.2023.111067>.
- [11] D. Chhala, J.-M. Giraudon, N. Nuns, M. Labaki, J.-F. Lamonier, Highly active noble-metal-free copper hydroxyapatite catalysts for the total oxidation of toluene, *ChemCatChem* 9 (12) (2017) 2275–2283, <https://doi.org/10.1002/cctc.201601714>.
- [12] V.K. Velisoju, H.P. Aytam, V. Akula, Selective hydrogenation and dehydrogenation using hydroxyapatite-based catalysts, in: *Design and Applications of Hydroxyapatite-Based Catalysts*, John Wiley & Sons Ltd, 2022, pp. 241–268.
- [13] Alumina/TiO₂/hydroxyapatite interface nanostructure composite filters as efficient photocatalysts for the purification of air in: *Reaction Kinetics, Mechanisms and Catalysis Volume 107 Issue 1* (2012). Accessed: March 22, 2023. [Online]. Available: <https://akjournals.com/view/journals/11144/107/1/article-p89.xml>.
- [14] Evaluation of the Oxygen Mobility in CePO₄-Supported Catalysts: Mechanistic Implications on the Water–Gas Shift Reaction | *The Journal of Physical Chemistry C*. Accessed: Mar. 22, 2023. [Online]. Available: <https://pubs.acs.org/doi/abs/10.1021/acs.jpcc.0c03649>.
- [15] Graphene/hydroxyapatite nano-composite for enhancement of hydrogen productivity from delignified duckweed - ScienceDirect. Accessed: Mar. 22, 2023. [Online]. Available: <https://www.sciencedirect.com/science/article/abs/pii/S0016236122023705>.
- [16] T.S. Trung, et al., Valorization of fish and shrimp wastes to nano-hydroxyapatite/chitosan biocomposite for wastewater treatment, *J. Sci.: Adv. Mater. Devices* 7 (4) (2022), 100485, <https://doi.org/10.1016/j.jsamd.2022.100485>.
- [17] “Eggshell waste: An effective source of hydroxyapatite for photocatalyst | *Journal of Metals, Materials and Minerals*.” Accessed: Mar. 22, 2023. [Online]. Available: <https://jmmm.material.chula.ac.th/index.php/jmmm/article/view/360>.
- [18] A. Srivastava, R.M. Rani, D.S. Patle, S. Kumar, Emerging bioremediation technologies for the treatment of textile wastewater containing synthetic dyes: a comprehensive review, *J. Chem. Technol. Biotechnol.* 97 (1) (2022) 26–41, <https://doi.org/10.1002/jctb.6891>.
- [19] K. Maheshwari, M. Agrawal, A.B. Gupta, “Dye Pollution in Water and Wastewater”, in *Novel Materials for Dye-containing Wastewater Treatment*, in: S.S. Muthu, A. Khadir (Eds.), *Sustainable Textiles: Production, Processing, Manufacturing & Chemistry*, Springer, Singapore, 2021, pp. 1–25, https://doi.org/10.1007/978-981-16-2892-4_1.
- [20] D.A. Yaseen, M. Scholz, Textile dye wastewater characteristics and constituents of synthetic effluents: a critical review, *Int. J. Environ. Sci. Technol.* 16 (2) (2019) 1193–1226, <https://doi.org/10.1007/s13762-018-2130-z>.
- [21] E. Hoseinzadeh, A. Rezaee, Electrochemical degradation of RB19 dye using low-frequency alternating current: effect of a square wave, *RSC Adv.* 5 (117) (2015) 96918–96926, <https://doi.org/10.1039/C5RA19686H>.
- [22] S. Sudarshan, et al., Impact of textile dyes on human health and bioremediation of textile industry effluent using microorganisms: current status and future prospects,

- J. Appl. Microbiol. 134 (2) (2023), Ixacc064, <https://doi.org/10.1093/jambio/ixacc064>.
- [23] B. Lellis, C.Z. Fávoro-Polonio, J.A. Pamphile, J.C. Polonio, Effects of textile dyes on health and the environment and bioremediation potential of living organisms, *Biotechnol. Res. Innovat.* 3 (2) (2019) 275–290, <https://doi.org/10.1016/j.biori.2019.09.001>.
- [24] Q. Liu, Pollution and treatment of dye waste-water, *IOP Conf. Ser.: Earth Environ. Sci.* 514 (5) (2020) 052001, <https://doi.org/10.1088/1755-1315/514/5/052001>.
- [25] Y.S. Hao, N. Othman, M.A.A. Zaini, Methylene blue and Congo red removal by activated carbons: a current literature, *Acta Universitatis Sapientiae, Agriculture and Environment* 14 (1) (2022) 29–44, <https://doi.org/10.2478/ausae-2022-0003>.
- [26] K. Manzoor, M. Batool, F. Naz, M.F. Nazar, B.H. Hameed, M.N. Zafar, A comprehensive review on application of plant-based bioadsorbents for Congo red removal, *Biomass Conv. Bioref.* (2022), <https://doi.org/10.1007/s13399-022-02741-5>.
- [27] "Development of nanoporous textile sludge based adsorbent for the dye removal from industrial textile effluent - ScienceDirect." Accessed: Mar. 22, 2023. [Online]. Available: <https://www.sciencedirect.com/science/article/abs/pii/S030438942101832X>.
- [28] "Augmented Biodegradation of Textile Azo Dye Effluents by Plant Endophytes: A Sustainable, Eco-Friendly Alternative | SpringerLink." Accessed: Mar. 22, 2023. [Online]. Available: <https://link.springer.com/article/10.1007/s00284-020-02202-0>.
- [29] "Microalgae biosorption, bioaccumulation and biodegradation efficiency for the remediation of wastewater and carbon dioxide mitigation: Prospects, challenges and opportunities - ScienceDirect." Accessed: Mar. 22, 2023. [Online]. Available: <https://www.sciencedirect.com/science/article/abs/pii/S2214714421000969>.
- [30] "Adsorptive Behavior of Methylene Blue onto Sawdust of Sour Lemon, Date Palm, and Eucalyptus as Agricultural Wastes: Journal of Dispersion Science and Technology: Vol 40, No 7." Accessed: Mar. 22, 2023. [Online]. Available: <https://www.tandfonline.com/doi/10.1080/01932691.2018.1489828>.
- [31] M.S. Hossain, S.M. Tuntun, N.M. Bahadur, S. Ahmed, Enhancement of photocatalytic efficacy by exploiting copper doping in nano-hydroxyapatite for degradation of Congo red dye, *RSC Adv.* 12 (52) (2022) 34080–34094.
- [32] M. Hossain, M. Mahmud, M.B. Mobarak, S. Ahmed, Crystallographic analysis of biphasic hydroxyapatite synthesized by different methods: an appraisal between new and existing models, *Chem. Pap.* (2021) 1–13.
- [33] M.S. Hossain, M.A.A. Shaikh, M.S. Rahaman, S. Ahmed, Modification of the crystallographic parameters in a biomaterial employing a series of gamma radiation doses, *Mol. Syst. Des. Eng.* 7 (10) (2022) 1239–1248, <https://doi.org/10.1039/D2ME00061J>.
- [34] M.S. Hossain, M. Mahmud, M.B. Mobarak, S. Sultana, M.A.A. Shaikh, S. Ahmed, New analytical models for precise calculation of crystallite size: application to synthetic hydroxyapatite and natural eggshell crystalline materials, *Chem. Pap.* 76 (2022) 7245–7251, <https://doi.org/10.1007/s11696-022-02377-9>.
- [35] M.S. Hossain, S.A. Jahan, S. Ahmed, Crystallographic characterization of bio-waste material originated CaCO₃, green-synthesized CaO and Ca (OH) 2, *Results Chem.* (2023), 100822.
- [36] M. Hossain, M. Hasan, M. Mahmud, M.B. Mobarak, S. Ahmed, Assessment of crystallite size of UV-synthesized hydroxyapatite using different model equations, *Chem. Pap.* (2022) 1–9.
- [37] I.G. Shitu, et al., X-ray diffraction (XRD) profile analysis and optical properties of Klockmannite copper selenide nanoparticles synthesized via microwave assisted technique, *Ceram. Int.* 49 (8) (2023) 12309–12326.
- [38] M. Sanaei-Moghadam, F. Vafaei, M. Jahangiri, F. Hormozi, M.A. Mahdi, M. Salavati-Niasari, Evaluation of the effect of maltodextrin and hydroxyethyl cellulose solution containing ZnO and Fe₂O₃ nanoparticles on the CO₂ release in sodium bicarbonate coating process, *Fuel* 331 (2023), 125522.
- [39] M. Aftab, A. Aftab, M.Z. Butt, D. Ali, F. Bashir, S.S. Iqbal, Surface hardness of pristine and laser-treated zinc as a function of indentation load and its correlation with crystallite size valued by Williamson-Hall analysis, size-strain plot, Halder-Wagner and Wagner-Aqua models, *Mater. Chem. Phys.* 295 (2023), 127117.
- [40] N.T. Tayade, M.P. Tirdude, Frustrated microstructures composite PbS material's size perspective from XRD by variant models of Williamson-Hall plot method, *Bull. Mater. Sci.* 46 (1) (2023) 20.
- [41] R.A. Parry, K. Ravichandran, Structural, thermal, electrical and magnetic properties of Fe₂CrAl FulHeusler alloy prepared by ball milling, *Phys. B Condens. Matter* (2023), 414665.
- [42] C.M. Ma, G.B. Hong, S.C. Lee, Facile synthesis of tin dioxide nanoparticles for photocatalytic degradation of congo red dye in aqueous solution, *Catalysts* 10 (7) (2020), 7, <https://doi.org/10.3390/catal10070792>.
- [43] I.D. Smičiklas, S.K. Milonjić, P. Pfenđ, S. Raićević, The point of zero charge and sorption of cadmium (II) and strontium (II) ions on synthetic hydroxyapatite, *Sep. Purif. Technol.* 18 (3) (2000) 185–194.
- [44] P.R. Maddigapu, V. Akula, M. Subrahmanyam, Hydroxyapatite photocatalytic degradation of calmagite (an azo dye) in aqueous suspension, *Appl. Catal. B-Environ.* 69 (2007) 164–170, <https://doi.org/10.1016/j.apcatb.2006.07.003>.
- [45] K. Teraoka, T. Nonami, Y. Yokogawa, H. Taoda, T. Kameyama, Preparation of TiO₂-coated hydroxyapatite single crystals, *J. Mater. Res.* 15 (6) (2000) 1243–1244.
- [46] K.W. Goh, et al., Effect of pH on the properties of eggshell-derived hydroxyapatite bioceramic synthesized by wet chemical method assisted by microwave irradiation, *Ceram. Int.* 47 (7, Part A) (2021) 8879–8887, <https://doi.org/10.1016/j.ceramint.2020.12.009>.